ACS ENVIRONMENTAL Au
AN OPEN ACCESS JOURNAL OF THE AMERICAN CHEMICAL SOCIETY

pubs.acs.org/environau Article

# Unlocking High-Efficiency Methane Oxidation with Bimetallic Pd−Ce Catalysts under Zeolite Confinement

Xiaomai Chen, Xuefeng Shi, Peirong Chen, Bowen Liu, Meiyin Liu, Longwen Chen, Daiqi Ye, Xin Tu,* Wei Fan,* and Junliang Wu*

Cite This: https://doi.org/10.1021/acsenvironau.3c00008 Read Online

ACCESS | Metrics & More | Article Recommendations | Supporting Information

**ABSTRACT:** Catalytic complete oxidation is an efficient approach to reducing methane emissions, a significant contributor to global warming. This approach requires active catalysts that are highly resistant to sintering and water vapor. In this work, we demonstrate that Pd nanoparticles confined within silicalite-1 zeolites (Pd@S-1), fabricated using a facile in situ encapsulation strategy, are highly active and stable in catalyzing methane oxidation and are superior to those supported on the S-1 surface due to a confinement effect. The activity of the confined Pd catalysts was further improved by co-confining a suitable amount of Ce within the S-1 zeolite ($PdCe_{0.4}$@S-1), which is attributed to confinement-reinforced Pd−Ce interactions that promote the formation of oxygen vacancies and highly reactive oxygen species. Furthermore, the introduction of Ce improves the hydrophobicity of the S-1 zeolite and, by forming Pd−Ce mixed oxides, inhibits the transformation of the active PdO phase to inactive $Pd(OH)_2$ species. Overall, the bimetallic $PdCe_{0.4}$@S-1 catalyst delivers exceptional outstanding activity and durability in complete methane oxidation, even in the presence of water vapor. This study may provide new prospects for the rational design of high-performance and durable Pd catalysts for complete methane oxidation.

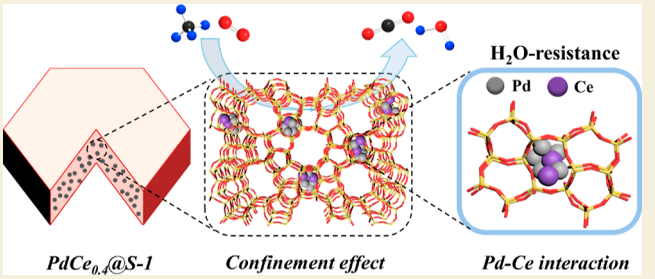


**KEYWORDS:** *catalytic methane oxidation, silicalite-1 zeolite, bimetallic Pd catalysts, confinement, Pd−Ce interaction*



## 1. INTRODUCTION

Methane ($CH_4$) is the main component of natural gas and is extensively used in power generation and other heating applications due to its high energy density and low emission of gaseous pollutants.[1−3] However, as one of the most predominant greenhouse gases, methane has a global warming potential 105 and 28 times stronger than that of $CO_2$ on a 20 year and 100 year scale, respectively.[4,5] Therefore, increasing attention has been given to strategies for the reduction of unburned methane emissions. Catalytic complete oxidation has been proven to be a promising technology with both environmental and economic benefits in minimizing $CH_4$ emissions and the resulting atmospheric pollution.[6−8] Nonetheless, it remains a great challenge to lower the ignition temperature of $CH_4$ oxidation to 400 °C and below, primarily due to the extremely stable and highly symmetrical structure of the $CH_4$ molecule.[1,9]

Pd-based catalysts have demonstrated excellent ability to activate C−H bonds of $CH_4$ and are among the most active catalysts for complete $CH_4$ oxidation.[10−12] However, the rapid deactivation induced by Pd sintering under real conditions (especially in the presence of steam) is one of the obstacles to the extensive applications of Pd catalysts.[13,14] To address this, confining ultrasmall Pd nanoparticles (NPs) into microporous zeolites with well-defined channels has been proven to be an effective strategy to suppress the agglomeration and sintering of Pd NPs and to maintain their catalytic performance in $CH_4$ oxidation.[15−19] For example, a Pd catalyst encapsulated in silicate-1 (Pd@S-1) at a low Pd loading of 0.6 wt % achieved a complete combustion temperature ($T_{100}$) of 380 °C, as well as excellent water resistance was achieved over a Pd catalyst encapsulated in silicate-1 (Pd@S-1) at a low Pd loading of only 0.6 wt %, due to a strong confinement effect and the high hydrophobicity of the S-1 zeolites.[16] The introduction of a second nonprecious metal can further promote the activity and stability of Pd catalysts.[20−23] Shi et al. and co-workers incorporated a series of metals (La, Ce, Sm, Nd, and Tb) into Pd/H-ZSM-5 for methane oxidation and decreased the $T_{100}$ by 40 °C in methane oxidation.[24] They found that Ce incorporation could weaken the Pd−O bond in Pd/H-ZSM-5, resulting in an improved reactivity of surface oxygen species. In addition, the excellent redox properties and oxygen storage capacity of $CeO_2$ are also favorable for $CH_4$ oxidation.[3,25,26]

Received: March 23, 2023
Revised: May 3, 2023
Accepted: May 4, 2023
Published: May 16, 2023

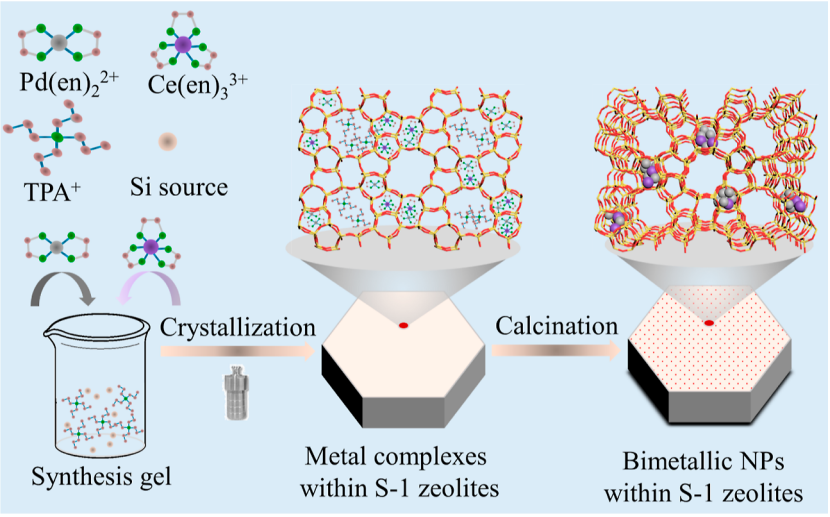


**Figure 1.** Schematic illustration of the preparation of $PdCe_x$@S-1.

Recently, Peng et al. demonstrated that core−shell PdCe@$SiO_2$ catalysts displayed both superior activity and outstanding $H_2O$ and $SO_2$ tolerance in $CH_4$ oxidation due to the strong interactions between Pd and $CeO_2$.[27]

Herein, we developed zeolite-confined bimetallic Pd−Ce catalysts by encapsulating Pd−Ce mixed oxides within hydrophobic S-1 zeolites using a one-pot hydrothermal method to take advantage of the confinement effect and Pd−$CeO_2$ interaction in $CH_4$ combustion. The resulting $PdCe_x$@S-1 catalysts exhibited superior performance in $CH_4$ oxidation, with increased activity and $H_2O$ tolerance. Comparative investigations using high-resolution transmission electron microscopy (HRTEM) together with ultramicrotomy, X-ray photoelectron spectroscopy (XPS), $O_2$-temperature-programed desorption ($O_2$-TPD), and diffuse reflection infrared Fourier transform spectroscopy with CO as the probe molecule (CO-DRIFTS) revealed that the cooperative effects of confinement and Pd−$CeO_2$ interactions are crucial for the high performance of the $PdCe_x$@S-1 catalysts. In situ DRIFTS was used to monitor of the intermediates during $CH_4$ oxidation to illustrate the reaction mechanisms over the bimetallic catalysts.

## 2. EXPERIMENTAL SECTION

### 2.1. Catalyst Preparation

S-1 zeolite-encapsulated bimetallic Pd−Ce oxides with different Ce/Pd molar ratios were synthesized via a hydrothermal method, as illustrated in Figure 1. For comparison, monometallic Pd@S-1 and Ce@S-1 catalysts were prepared by the same method, and Pd/S-1 and $PdCe_{0.4}$/S-1 samples were synthesized using an incipient wetness impregnation (IWI) method.

The S-1 zeolite was synthesized according to previously published literature.[28] First, 13 g of tetrapropylammonium hydroxide (TPAOH) solution was mixed with 15.45 g of deionized water at room temperature and stirred for 15 min. Then, 8.32 g of tetraethyl orthosilicate was added dropwise into the above mixture with a continuous stirring for 6 h. Finally, the obtained zeolite precursor gel with a molar ratio of 1 $SiO_2$/0.4 TPAOH/35 $H_2O$ was poured into a 100 mL Teflon-lined stainless-steel autoclave and hydrothermally treated in an oven at 170 °C for 4 days under static conditions. The as-synthesized solid sample was washed by centrifugation with water and ethanol several times and then dried overnight at 80 °C, followed by calcination in air at 550 °C for 8 h at a heating ramp of 1 °C $min^{-1}$.

Before preparing the $PdCe_x$@S-1 catalyst, a solution of $[Pd(NH_2CH_2CH_2NH_2)_2]Cl_2$ was prepared by dissolving 0.20 g of $PdCl_2$ in a mixture of 1 mL of ethylenediamine and 4 mL of water. Similarly, 0.42 g of $CeCl_3{\cdot}7H_2O$ was added to the same mixture to obtain the $[Ce(NH_2CH_2CH_2NH_2)_3]Cl_3$ solution. $PdCe_x$@S-1 and Ce@S-1 were synthesized using the same process as S-1 zeolite, but with the addition of $[Pd(NH_2CH_2CH_2NH_2)_2]Cl_2$ and/or $[Ce(NH_2CH_2CH_2NH_2)_3]Cl_3$ to the precursor gel. To prepare $PdCe_x$@S-1, 1.2 mL of $[Pd(NH_2CH_2CH_2NH_2)_2]Cl_2$ solution and $x$ mL ($x$ = 0, 1, 2, 4) of $[Ce(NH_2CH_2CH_2NH_2)_3]Cl_3$ were added dropwise to the synthesis mixture and stirred continuously for 1 h. Ce@S-1 was synthesized using 1 mL of $[Ce(NH_2CH_2CH_2NH_2)_3]Cl_3$ under the same conditions. The resulting gel, with a molar ratio of 1.0 $SiO_2$/0.4 TPAOH/35 $H_2O$: 0.0075 $[Pd(NH_2CH_2CH_2NH_2)_2]Cl_2$/$y$ $[Ce(NH_2CH_2CH_2NH_2)_3]Cl_3$ ($y$ = 0, 0.003, 0.00675, 0.0165) was transferred into a 100 mL Teflon-lined stainless-steel autoclave and heated to 170 °C for 4 days under static conditions. Finally, the as-synthesized catalysts were centrifuged, washed, and dried under the same conditions as the S-1 preparation. The collected solid catalysts were then calcined at 550 °C for 8 h in air.

The Pd/S-1 catalyst was prepared using the IWI method, which involved using a solution of $(NH_4)_2PdCl_4$. Specially, 1 g of calcined S-1 zeolite was impregnated with 2.67 mL of $(NH_4)_2PdCl_4$ (0.05 M) and placed in ultrasonication for 2 h to improve the dispersion of the metal on the S-1 zeolite. The resulting suspension was then dried at 80 °C overnight and subsequently calcined at 550 °C in air for 8 h. $CeCl_3{\cdot}7H_2O$ was used as the source of Ce to synthesize $PdCe_{0.4}$/S-1, following the same procedure as for $PdCe_x$@S-1.

### 2.2. Catalyst Characterization

Comprehensive catalyst characterizations were carried out for all catalysts, including thermal gravimetric analysis (TGA, Figure S1), inductively coupled plasma−mass spectrometry (ICP−MS), powder X-ray diffraction (PXRD), $N_2$ physisorption isotherms, thermal gravimetric analysis, TEM, high-angle annular dark-field (HAADF) and elemental mapping, CO chemisorption, XPS, Raman spectroscopy, $O_2$-TPD, electron paramagnetic resonance (EPR), methane temperature-programed reaction ($CH_4$-TPR), and in situ DRIFTS. Detailed procedures for these characterizations are provided in the Supporting Information.

### 2.3. Catalytic Evaluation

The activities of $PdCe_x$@S-1 and reference catalysts in $CH_4$ combustion were tested at atmospheric pressure using a quartz fixed-bed flow reactor. Typically, 100 mg of catalyst (40−60 mesh) was mixed with 400 mg of quartz sand and placed in the middle of a quartz tube that was blocked by silica wool. The reactant gas containing 1.0 vol % $CH_4$, 20 vol % $O_2$, and balanced with $N_2$ was flowed through the reactor at a total flow rate of 100 mL $min^{-1}$, corresponding to a gas hourly space velocity (GHSV) of 60,000 mL $g^{-1}$ $h^{-1}$. The temperature of the reactor was then programed from room temperature to 440 °C at intervals of 20 °C, with


https://doi.org/10.1021/acsenvironau.3c00008
ACS Environ. Au XXXX, XXX, XXX−XXX

each temperature held for 30 min. The inlet and outlet gas concentrations of $CH_4$ were detected by an online gas chromatograph (GC-2014, Japan) equipped with a thermal conductivity detector (TCD) and a flame ionization detector (FID).

The conversion of $CH_4$ ($X_{CH_4}$) was calculated according to the following equations

$$X_{CH_4}(\%) = \frac{CH_{4,in} - CH_{4,out}}{CH_{4,in}} \times 100 \quad (1)$$

where $CH_{4,in}$ and $CH_{4,out}$ are the inlet and outlet concentrations of $CH_4$, respectively.

Kinetic measurements were further performed by controlling the temperature between 200 and 260 °C to maintain $CH_4$ conversions below 15% in order to eliminate the limitations of heat and mass transfer. The $CH_4$ reaction rate ($r_{CH_4}$) and the turnover frequencies (TOF) were estimated using the following equations

$$r_{CH_4}(\text{mol } g_{Pd}^{-1}\ s^{-1}) = \frac{c_{CH_4} X_{CH_4} VP_{atm}}{m_{cat}\omega_{Pd}RT} \quad (2)$$

$$\text{TOF } (s^{-1}) = \frac{r_{CH_4} M_{Pd}}{D_{Pd}} \quad (3)$$

where $c_{CH_4}$ is the $CH_4$ concentration in the feed gas, $V$ is the total flow rate, $P_{atm}$ is the atmospheric pressure (101.3 kPa), $m_{cat}$ is the catalyst mass used for the measurement, $\omega_{Pd}$ is the Pd loading measured by ICP, $R$ is the molar gas constant (8.314 Pa $m^3$ $mol^{-1}$ $K^{-1}$), $T$ is the temperature (298 K), and $M_{Pd}$ is the atomic weight of Pd (106.4 g $mol^{-1}$). $D_{Pd}$ is the dispersion of Pd measured by CO chemisorption (Table 1). Moreover, the apparent activation energy (Ea) values were calculated using the Arrhenius equation by plotting ln ($r_{CH_4}$) vs 1000/$T$.

**Table 1. Elemental Composition, Specific Surface Area, Size, and Dispersion of Metal NPs**

| samples | Pd loading (wt %)[a] | Ce loading (wt %) | $S_{BET}$ ($m^2$ $g^{-1}$)[b] | Pd dispersion (%)[c] |
|---|---|---|---|---|
| Pd/S-1 | 1.07 | | 387 | 15.2 |
| Pd@S-1 | 1.00 | | 389 | 19.7 |
| $PdCe_{0.4}$@S-1 | 1.09 | 0.58 | 386 | 26.2 |

[a]Measured by ICP−MS. [b]Obtained from BET. [c]Calculated by CO chemisorption (sample was pretreated at 300 °C for 1 h in 10 vol % $H_2$/Ar).

To evaluate the temperature tolerance of the representative catalysts ($PdCe_{0.4}$@S-1, Pd@S-1, and Pd/S-1), a temperature cycle of 300 → 600 → 300 °C was performed with an interval of 100 °C for 10 h. The stability test of the catalysts was then tested for at least 40 h at 310 °C under dry conditions. In addition, 5.0 vol % water vapor was introduced using a bubbling device to explore the water resistance ability of the catalysts. The GHSV was kept consistent in all tests.

## 3. RESULTS AND DISCUSSION

### 3.1. Structural Characterization

The actual Pd and Ce loadings in $PdCe_x$@S-1 ($x$ denotes the Ce/Pd molar ratio), Pd/S-1, and $PdCe_{0.4}$/S-1 were determined by ICP−MS, and the results are summarized in Tables 1 and S1. The Pd contents in all the samples are similar (1.0 wt %), and the Ce/Pd molar ratios are 0.4, 0.9, and 2.2 for $PdCe_{0.4}$@S-1, $PdCe_{0.9}$@S-1, and $PdCe_{2.2}$@S-1, respectively. According to PXRD (Figure S2), all the samples present the typical MFI topology structure (JCPDS 44-0003) and good crystallinity, indicating that the introduction of Pd or Ce phase did not affect the zeolite crystallization. Moreover, no characteristic diffraction peaks of Pd or Ce species were detected, implying good dispersions of Pd and Ce species within the zeolite. The Brunauer−Emmett−Teller (BET) surface areas (Figure S3 and Tables 1 and S2) were found to be similar (ca. 380 ± 10 $m^2$ $g^{-1}$) for all the Pd-contained and Pd-free S-1 samples. However, a decrease in micropore volume was noticed in Pd@S-1 (0.07 $cm^3$ $g^{-1}$) and $PdCe_{0.4}$@S-1 (0.09 $cm^3$ $g^{-1}$) compared with pure S-1 zeolite (0.13 $cm^3$ $g^{-1}$), likely due to the partial occupation of the micropores by PdO NPs.[17,28]

XPS analysis was conducted to determine the chemical nature of Pd and Ce in these catalysts (Figures 2d and S4). While intense peaks at 336.79 and 341.96 eV attributed to Pd $3d_{5/3}$ and Pd $3d_{3/2}$ of PdO were observed in the Pd/S-1 sample prepared by the IWI method,[29] no obvious Pd 3d signal was detected over Pd@S-1 and $PdCe_{0.4}$@S-1 with similar Pd loadings as Pd/S-1. This finding further proves the complete confinement of PdO NPs and bimetallic Pd−Ce oxide NPs inside the S-1 zeolites for the two catalysts (Pd@S-1 and $PdCe_{0.4}$@S-1). After argon ion sputtering, which was used to obtain the valence of Pd and Ce atoms within zeolite, clear peaks appeared at 336.0 (Pd $3d_{5/2}$) and 341.15 eV (Pd $3d_{3/2}$), suggesting the exposure of PdO species that were detectable by XPS (Figure 2d). Interestingly, compared to Pd@S-1, the Pd $3d_{5/2}$ and $3d_{3/2}$ positions of $PdCe_{0.4}$@S-1 (336.35 and 341.5 eV) shifted to higher values, which can be ascribed to strong interactions between PdO and $CeO_2$, leading to more electron deficiency of the Pd atoms.[20] The predominant presence of PdO, widely accepted as the active phase for $CH_4$ activation,[30,31] is thus expected to favor the complete $CH_4$ oxidation reaction.

The TEM images shown in Figure S5 confirm the typical hexagonal morphology of S-1 crystals, with a size of 200−400 nm observed in all the catalysts. To identify the exact locations of PdO NPs in S-1 (i.e., Pd@S-1 and $PdCe_{0.4}$@S-1), an ultramicrotomy method (Figure 2a) was adopted to prepare specimen for TEM analysis. Specifically, the zeolite crystals embedded in resin were cut into 90 nm thick ultrathin slices by ultramicrotome, and thereby the exposed cross-sections of the zeolite crystal were analyzed to obtain information about the spatial distribution of metal species inside the crystals.[32] The ultramicrotomy HRTEM images (Figure 2b,e) verifiably depict that the ultrasmall PdO NPs and Pd−Ce bimetallic oxide NPs were uniformly dispersed throughout the S-1 zeolites in Pd@S-1 and $PdCe_{0.4}$@S-1, respectively. The corresponding average particle sizes of the metal oxides (PdO or Pd−Ce bimetallic oxide) were obtained by measuring more than 200 particles and found to be around 2.1 and 2.4 nm for Pd@S-1 and $PdCe_{0.4}$@S-1, respectively (Figure 2c,f). By stark contrast, the image of PdO NPs in Pd/S-1 prepared by the IWI method was severely sintered and agglomerated with an uneven size distribution (Figure 2g,h), with some PdO particles even larger than 10 nm (red circles). The above HRTEM analysis signifies that the in situ encapsulation method could inhibit Pd aggregation and improve Pd dispersion. CO chemisorption experiments revealed a sequence of Pd dispersion (Table 1 and Figure S6) following: $PdCe_{0.4}$@S-1 (26.2%) > Pd@S-1 (19.7%) > Pd/S-1 (15.2%), in good agreement with the TEM results. Elemental distribution in the $PdCe_{0.4}$@S-1 (ultramicrotomy) was further measured using HAADF-STEM and EDX mapping (Figure 2i−n). Both Pd and Ce elements were evenly located at nearly identical positions, suggesting that both of Pd and Ce atoms were encapsulated into the zeolite matrix. Line scan analysis presents similar signal intensities of Pd and Ce (Figure S7), implying the formation of a bimetallic Pd−Ce oxide phase in the $PdCe_{0.4}$@S-1 catalyst.


https://doi.org/10.1021/acsenvironau.3c00008
ACS Environ. Au XXXX, XXX, XXX−XXX

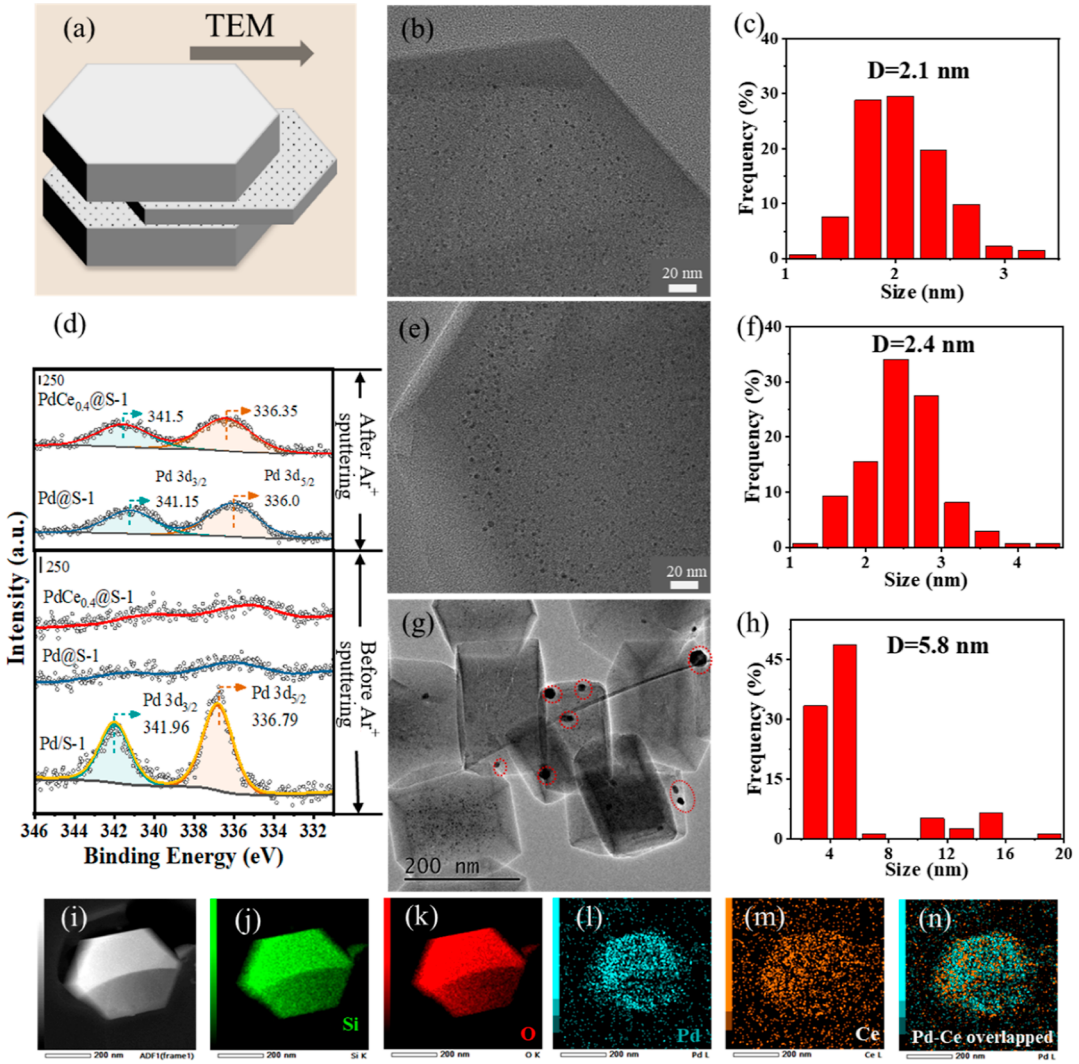


**Figure 2.** (a) Schematic illustration of the ultramicrotomy method. HRTEM images and size distributions of PdO or PdCe bimetallic oxide NPs for (b,c) Pd@S-1, (e,f) $PdCe_{0.4}$@S-1, and (g,h) Pd/S-1. (d) Pd 3d XPS spectra of Pd/S-1, Pd@S-1, and $PdCe_{0.4}$@S-1 before and after $Ar^+$ ion sputtering. (i–n) HAADF-STEM images and elemental mappings for Si, O, Pd, and Ce of $PdCe_{0.4}$@S-1 (ultramicrotomy).

### 3.2. Catalytic Performance in Complete $CH_4$ Oxidation

The catalytic activities of all the Pd catalysts for complete $CH_4$ oxidation were measured and compared in Figures 3a and S8 and S9. Figure S10 shows the reaction temperatures required to achieve $CH_4$ conversions of 10, 50, 90, and 100%, denoted as $T_{10}$, $T_{50}$, $T_{90}$, and $T_{100}$, respectively. The reaction rates, apparent activation energies (Ea), and TOF values are presented in Figure 3b and Table 2. As shown in Figure 3a, Pd@S-1, containing confined PdO NPs (with $T_{100}$ at 370 °C), showed a much better activity than Pd/S-1 ($T_{100}$ = 430 °C), which has PdO NPs on the zeolite surface. Notably, Pd@S-1 also has a lower Ea (88.9 kJ $mol^{-1}$) than that of Pd/S-1(96.0 kJ $mol^{-1}$), emphasizing the importance of the confinement effect in $CH_4$ oxidation. According to TEM and CO chemisorption (Table 1), the in situ encapsulation method significantly increased Pd dispersion compared with the IWI method, leading to a higher density of accessible Pd sites in Pd@S-1, which are intrinsically beneficial for activating $CH_4$ molecules.

Co-confining a small amount of Ce further decreased the $T_{100}$ of Pd@S-1. However, when an excess amount of Ce was added, it was found to be detrimental to $CH_4$ oxidation, as indicated by the unexpected increase of $T_{100}$. Ultimately, the optimal Ce/Pd molar ratio was found to be 0.4 ($PdCe_{0.4}$@S-1), with a $T_{100}$ of 350 °C and an Ea value of 83.2 kJ $mol^{-1}$ (about 20 °C and 5.7 kJ $mol^{-1}$ lower than those of Pd@S-1, respectively; Table 2). It should be noted that Ce@S-1 displayed hardly any $CH_4$ oxidation activity below 440 °C, suggesting that pure Ce species confined in S-1 are not active in $CH_4$ oxidation (Figure S9). At 240 °C, the reaction rate of $PdCe_{0.4}$@S-1 was found to be 1.5 times higher than that of Pd@S-1, and the TOF value of $PdCe_{0.4}$@S-1 (0.037 $s^{-1}$) was also the highest among all the Pd catalysts (Table 2). On the other hand, $PdCe_{0.4}$/S-1 prepared by the IWI method, despite having the same Ce/Pd molar ratio as that of $PdCe_{0.4}$@S-1, showed much lower activity in $CH_4$ oxidation ($T_{100}$ = 440 °C). Furthermore, $PdCe_{0.4}$@S-1 also exhibited better catalytic activity than as-prepared $Pd/Al_2O_3$, Pd/SSZ-13, and $Pd/SiO_2$ catalysts (all with Pd loadings of 2 wt %) in Figure S9. These results indicate that the confinement effect of S-1 zeolite induces a synergy between Pd and Ce and decreases the energy barrier of $CH_4$ oxidation. In fact, $PdCe_{0.4}$@S-1 is one of the best catalysts for complete $CH_4$ oxidation as compared to state-of-the-art Pd catalysts reported in the literature (Table S3).


https://doi.org/10.1021/acsenvironau.3c00008
ACS Environ. Au XXXX, XXX, XXX−XXX

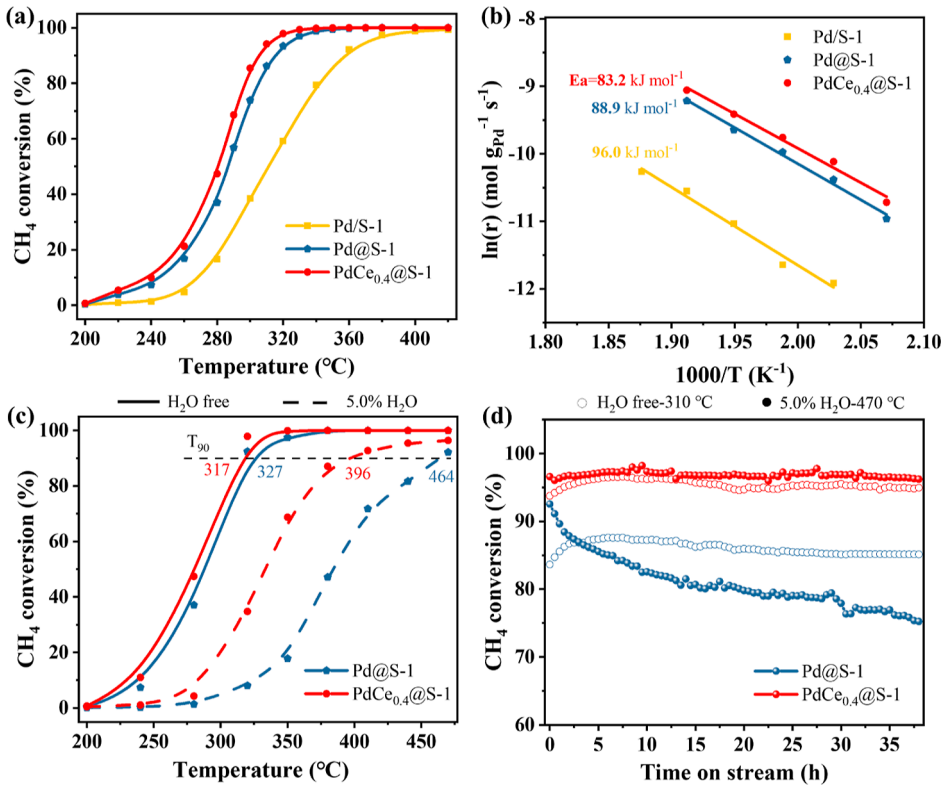


**Figure 3.** (a) $CH_4$ conversion, (b) Arrhenius plots (reaction conditions: 1.0 vol % $CH_4$, 20 vol % $O_2$, balanced with $N_2$, GHSV = 60,000 mL $g_{cat}^{-1}$ $h^{-1}$), (c) water resistance test, and (d) long-term stability without $H_2O$ at 310 °C and with $H_2O$ at 470 °C over Pd@S-1 and $PdCe_{0.4}$@S-1 (reaction conditions: 1.0 vol % $CH_4$, 20 vol % $O_2$, with or without 5.0% $H_2O$, balanced with $N_2$, GHSV = 60,000 mL $g_{cat}^{-1}$ $h^{-1}$).

**Table 2. Catalytic Performance of the Obtained Pd Catalysts in Complete $CH_4$ Oxidation**

| samples | $T_{100}$ (°C) | rate$^{@240\ °C}$ (mmol $g_{Pd}^{-1}s^{-1}$) | TOF$^{@240\ °C}$ ($10^{-2}s^{-1}$) | Ea (kJ $mol^{-1}$) |
|---|---|---|---|---|
| Pd/S-1 | 440 | 1.6 | 1.1 | 96.0 |
| Pd@S-1 | 370 | 6.0 | 3.2 | 88.9 |
| $PdCe_{0.4}$@S-1 | 350 | 9.2 | 3.7 | 83.2 |
| $PdCe_{2.2}$@S-1 | 410 | 3.2 | 1.4 | 90.8 |
| $PdCe_{0.4}$/S-1 | 440 | 0.92 | | 103.3 |

The Pd catalysts were also evaluated at high temperatures or in the presence of water vapor to explore their potential for real world applications where such harsh reaction conditions are commonly encountered (Figures S11 and S12).[17,33] As shown in Figure S11, the temperature tolerance of $PdCe_{0.4}$@S-1, Pd@S-1, and Pd/S-1 was evaluated, starting from 300 to 600 °C and then decreasing back to 300 °C. $PdCe_{0.4}$@S-1 and Pd@S-1 exhibited initially higher activity than Pd/S-1 as presented before (Figure 3a), demonstrating their outstanding temperature tolerance with the aid of a confined structure. TEM measurements were performed again on the Pd catalysts after the temperature tolerance tests. While a severe Pd sintering was observed over Pd/S-1 (with an increase in PdO particle size from 5.8 to 9.2 nm and the appearance of PdO NPs even larger than 20 nm; Figure S13), only slight increases in particle size were noted over Pd@S-1 (from 2.1 to 2.4 nm) and $PdCe_{0.4}$@S-1 (from 3.0 to 3.1 nm), confirming the effectiveness of confinement in preventing the agglomeration of Pd species. In addition, cycling experiments showed that $PdCe_{0.4}$@S-1 demonstrated similar activity over five cycles of $CH_4$ oxidation (Figure S12). TEM images showed that the metal particle size of the used catalysts increased slightly from 2.4 to 2.7 nm, suggesting the excellent stability of the $PdCe_{0.4}$@S-1 catalyst (Figure S14).

In the presence of water vapor (in the feed gas or from methane combustion), which is believed to accelerate the sintering of Pd-based catalysts,[34] the increase of $T_{90}$ was less significant in the case of $PdCe_{0.4}$@S-1 (by 90, or 306 to 396 °C) than Pd@S-1 (by 135 °C, or from 329 to 464 °C), indicating a stronger water resistance of $PdCe_{0.4}$@S-1 (Figure 3c). Interestingly, in the 40 h stability tests (Figure 3d), $PdCe_{0.4}$@S-1 maintained its activity under both dry (310 °C, no water vapor) and wet (470 °C, 5.0% water vapor) conditions, while Pd@S-1 gradually deactivated under wet conditions with a decrease of $CH_4$ conversion from 92 to 74% (although it displayed stable performance under dry conditions as well). It is known that high concentrations of water vapor could poison Pd catalysts by forming an inactive $Pd(OH)_2$ phase.[16,35,36] Therefore, the confinement effect of hydrophobicity in S-1 zeolite is not the main reason for the higher water tolerance of $PdCe_{0.4}$@S-1 compared to Pd@S-1. Instead, the Pd−$CeO_2$ interaction is believed to inhibit the reaction between Pd and water to generate $Pd(OH)_2$ in $PdCe_{0.4}$@S-1.[27] As shown in Figure S15, the Pd particle size of the used Pd@S-1 (after the water resistance experiment) increased by more than 1 nm (from 2.1 to 3.1 nm), while the used $PdCe_{0.4}$@S-1 only increased from 2.4 to 2.8 nm. This finding unambiguously indicates that the synergistic effect of Pd and $CeO_2$ in zeolite plays an important role in prohibiting the poison of water vapor on the active the Pd phase.

### 3.3. Mechanistic Investigations

**3.3.1. Role of Ce Co-confining.** The abovementioned results of $CH_4$ oxidation suggest a potential synergy between


https://doi.org/10.1021/acsenvironau.3c00008
ACS Environ. Au XXXX, XXX, XXX−XXX

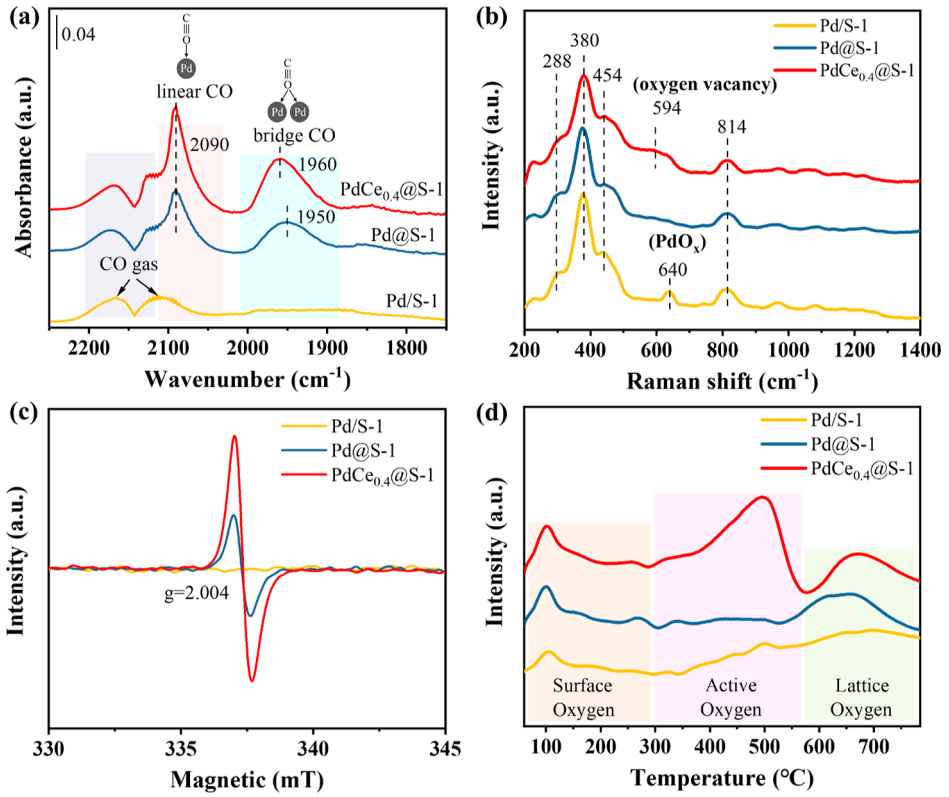


**Figure 4.** (a) CO-DRIFTS spectra (samples were pre-treated at 300 °C for 1 h in 10 vol % $H_2$/Ar), (b) UV Raman, (c) EPR, and (d) $O_2$-TPD of $PdCe_{0.4}$@S-1 and related catalysts.

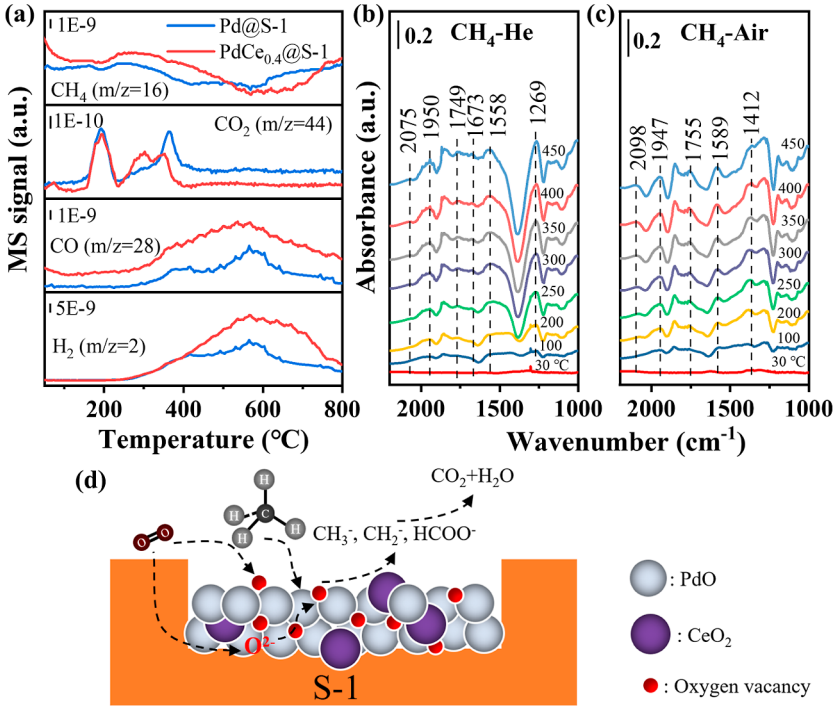


**Figure 5.** (a) $CH_4$-TPR profiles of $PdCe_{0.4}$@S-1 and Pd@S-1. In situ DRIFT spectra of $PdCe_{0.4}$@S-1 under (b) 1 vol % $CH_4$/He and (c) 1 vol % $CH_4$/Air flows at various temperatures and (d) schematic illustration of the possible reaction pathway of $CH_4$ oxidation over $PdCe_{0.4}$@S-1.

zeolite confinement and Ce co-confining in the $PdCe_{0.4}$@S-1 catalyst. To gain more insight into the reaction mechanism, we performed in situ CO-DRIFTS, UV Raman, EPR, and $O_2$-TPD analyses. $H_2$ pre-treatment was performed before the in situ CO-DRIFTS test to reduce the Pd cations into a metallic state, which enhances the adsorption capacity of probe molecules (CO) and increases the signal intensity.[20] This is because cationic Pd sites exhibit weaker interactions with CO molecules than metallic Pd sites.[37−40] As shown in Figure 4a, only two bands located at 2112 and 2172 $cm^{-1}$ for gaseous CO were observed over Pd/S-1,


https://doi.org/10.1021/acsenvironau.3c00008
ACS Environ. Au XXXX, XXX, XXX−XXX

which is due to CO adsorption on large Pd particles without confinement. In contrast, clear CO adsorption bands were observed at 2090 and 1950 $cm^{-1}$ over the encapsulated catalysts (i.e., Pd@S-1 and $PdCe_{0.4}$@S-1) and can be assigned to the linear and bridging stretching vibrations of CO adsorption on $Pd^0$ sites, respectively.[41] The increased intensity of linear CO adsorption on $PdCe_{0.4}$@S-1 is attributed to the formation of bimetallic Pd−Ce oxide NPs in the presence of a suitable amount of co-confined Ce species, which strengthened the CO adsorption on Pd sites.[42] It is well documented that such bimetallic Pd−Ce oxide NPs could facilitate the cleavage of C−H of $CH_4$ and enhance the activity of $CH_4$ oxidation.[26]

In the UV Raman spectra (Figure 4b), peaks related to the S-1 zeolite framework (ca. 288, 380, 454, 814 $cm^{-1}$) were detected in all the samples.[43] For Pd/S-1, an additional band at ca. 640 $cm^{-1}$ related to the $B_{1g}$ vibration mode of the PdO phase was observed and can be attributed to the aggregation of the PdO phase in the catalyst,[44] in line with TEM and CO DRIFTS observations. For $PdCe_{0.4}$@S-1, a band at 594 $cm^{-1}$ corresponding to a defect-induced (D) vibration mode was detected and is generally ascribed to oxygen vacancy sites in $CeO_2$.[45,46] EPR studies confirmed the presence of bulk oxygen vacancy defects in the $PdCe_{0.4}$@S-1 catalysts. As shown in Figure 4c, a symmetrical signal at $g$ = 2.004 ascribed to unpaired electrons in oxygen vacancies was visualized in the spectrum of $PdCe_{0.4}$@S-1.[47,48] The existence of oxygen vacancies is beneficial for the activation of gaseous $O_2$ molecules to generate reactive oxygen species capable of cleaving C−H bonds in $CH_4$.[49−51] Accordingly, $O_2$-TPD measurements were conducted to investigate the oxygen properties of $PdCe_{0.4}$@S-1 and related catalysts. Indeed, in the $O_2$-TPD profiles in Figure 4d, more intense oxygen desorption peaks were recorded at ca. 500 °C and ca. 650 °C, resulting from active species by the activation of surface lattice oxygen.[52] These active oxygen species are generally considered to favor $CH_4$ activation following the Mar−van Krevelen (M−vK) mechanism.[53] In $CH_4$-TPR experiments, we detected similar behaviors of $CH_4$ consumption and $CO_2$ formation in the absence of gas-phase $O_2$ at temperatures below 250 °C over the $PdCe_{0.4}$@S-1 and Pd@S-1 catalysts (Figure 5a). In the temperature range of 250−400 °C, CO formation was also detected, in addition to $CH_4$ consumption and $CO_2$ formation. The produced $CO/CO_2$ likely resulted from the reaction between $CH_4$ and active PdO species, as shown in the following equation

$$CH_4 + 4O_{PdO} \rightarrow CO_2/CO + 2H_2O \quad (4)$$

$CH_4$ consumption at high temperatures (400−800 °C) was accompanied by the formation of CO and $H_2$, which could be ascribed to the incomplete $CH_4$ oxidation ($CH_4 + 2O \rightarrow CO + 2H_2O$, $CH_4 + O \rightarrow CO + 2H_2$) and/or the $CH_4$ cracking ($CH_4 \rightarrow C + 2H_2$).[54,55] Notably, $PdCe_{0.4}$@S-1 shows a lower $CO_2$ formation temperature (centered at 320 °C) and a more intense peak of $CO_2$ formation compared with Pd@S-1, which, according to $O_2$-TPD, may result from a higher amount of active oxygen species after Ce co-confining.

**3.3.2. Reaction Pathway.** In situ DRIFTS was combined with $CH_4$-TPO to investigate the reaction intermediates during the catalytic $CH_4$ oxidation over $PdCe_{0.4}$@S-1, and the results are shown in Figures 5b,c and S16. Generally, the band intensity of $CH_4$ (3016 $cm^{-1}$) decreased with increasing temperature, while the bands at 1558 $cm^{-1}$ ascribed to formate species at 1558 $cm^{-1}$ appeared above 200 °C in $CH_4$/He.[30] Meanwhile, peaks attributed to the adsorbed bidentate carbonates (1673 $cm^{-1}$) and bicarbonates (1269 $cm^{-1}$) intermediates were also detected.[30,56] Interestingly, broad bands centered at 1950 and 2075 $cm^{-1}$ related to chemisorbed CO in bridging and linear forms, respectively, appeared and gradually increased in intensity with temperature, which is due to the direct reaction between $CH_4$ and the O species in PdO. The likely reaction process over $PdCe_{0.4}$@S-1 is: $CH_4 \rightarrow CH_4^* \rightarrow$ formate → bidentate carbonates/bicarbonates → CO → $CO_2$. In a $CH_4$ + air atmosphere, the bridge-adsorbed CO (1947 $cm^{-1}$) and linear-adsorbed CO (2098 $cm^{-1}$) bands also appeared (Figure 5c). Notably, the bands for adsorbed formate (1558 $cm^{-1}$) and bidentate carbonates (1673 $cm^{-1}$) intermediates vanished after the addition of air, while the bands for carboxylates (1589 $cm^{-1}$) and carbonate (1412 $cm^{-1}$) appeared,[30,57] indicating an accelerated transformation of formate to carbonate by $O_2$ injection. The reaction process thus changed to $CH_4 \rightarrow CH_4^*$ → carbonate → carboxylates → CO → $CO_2$.

Based on in situ DRIFTS, $CH_4$-TPR, and $O_2$-TPD results as well as published literature,[58,59] we propose the reaction pathway of $CH_4$ oxidation over $PdCe_{0.4}$@S-1 following the M-vK mechanism (Figure 5d), where the activation of the first C−H bond is the rate-determining step.[50] Initially, $CH_4$ is adsorbed on the active sites of bimetallic Pd−Ce mixed oxide inside the S-1 crystal and activated to methyl species and surface hydroxyl groups. Subsequently, the $CH_3^-$ and $CH_2^-$ species are oxidized by the active oxygen species to form carbonate and carboxylate intermediates, which are further oxidized to chemisorbed CO. Finally, the chemisorbed CO is transformed to $CO_2$ and $H_2O$ as the final products. Moreover, the diffusion of lattice oxygen from bulk or the adsorption of gas-phase $O_2$ would refill the oxygen vacancies of $PdCe_{0.4}$@S-1. It is known that the active lattice oxygen species play a crucial role when $CH_4$ oxidation follows the M-vK mechanism.[52,53] Therefore, $PdCe_{0.4}$@S-1 with more active oxygen species exhibits superiority in the oxidation of $CH_4$ to $CO_2$ and $H_2O$.

## 4. CONCLUSIONS

In summary, a bimetallic Pd−Ce oxide catalyst confined inside S-1 zeolite was successfully synthesized using a facile in situ encapsulation strategy and demonstrated superior catalytic activity (with a $T_{100}$ of 350 °C) and thermal stability in complete $CH_4$ oxidation. The confinement effect promoted the accessibility of highly dispersed active Pd sites and prevented sintering at high temperatures and/or in the presence of water vapor, while the introduction of Ce generated more oxygen vacancies and active oxygen species that are effective in $CH_4$ activation and oxidation. The strong interaction between Pd and Ce within the hydrophobic S-1 zeolite protected the active PdO phase from transformation into inactive $Pd(OH)_2$ in high-concentration water vapor, thus ensuring exceptional stability in $CH_4$ oxidation. These findings provide a perspective for the rational design and development of active and stable catalysts for complete $CH_4$ oxidation under harsh conditions.

## ■ ASSOCIATED CONTENT

### Supporting Information

The Supporting Information is available free of charge at https://pubs.acs.org/doi/10.1021/acsenvironau.3c00008.

Experimental details, additional catalyst characterization, additional catalytic performance, TEM images and size distribution of catalysts after reaction, additional in situ DRIFT spectra, additional information of catalysts, and


https://doi.org/10.1021/acsenvironau.3c00008
ACS Environ. Au XXXX, XXX, XXX−XXX

comparison of different catalysts for methane combustion (PDF)

## AUTHOR INFORMATION


### Corresponding Authors

**Xin Tu** − *Department of Electrical Engineering and Electronics, University of Liverpool, Liverpool L69 3GJ, U.K.;* orcid.org/0000-0002-6376-0897; Email: xin.tu@liverpool.ac.uk

**Wei Fan** − *Department of Chemical Engineering, University of Massachusetts—Amherst, Amherst, Massachusetts 01003, United States;* orcid.org/0000-0002-8581-2651; Email: wfan@ecs.umass.edu

**Junliang Wu** − *National Engineering Laboratory for VOCs Pollution Control Technology and Equipment, Guangdong Provincial Key Laboratory of Atmospheric Environment and Pollution Control, School of Environment and Energy, South China University of Technology, Guangzhou 510006, China;* orcid.org/0000-0002-6399-3770; Email: ppjl@scut.edu.cn

### Authors

**Xiaomai Chen** − *National Engineering Laboratory for VOCs Pollution Control Technology and Equipment, Guangdong Provincial Key Laboratory of Atmospheric Environment and Pollution Control, School of Environment and Energy, South China University of Technology, Guangzhou 510006, China;* orcid.org/0000-0003-3058-4900

**Xuefeng Shi** − *National Engineering Laboratory for VOCs Pollution Control Technology and Equipment, Guangdong Provincial Key Laboratory of Atmospheric Environment and Pollution Control, School of Environment and Energy, South China University of Technology, Guangzhou 510006, China*

**Peirong Chen** − *National Engineering Laboratory for VOCs Pollution Control Technology and Equipment, Guangdong Provincial Key Laboratory of Atmospheric Environment and Pollution Control, School of Environment and Energy, South China University of Technology, Guangzhou 510006, China;* orcid.org/0000-0003-1014-8044

**Bowen Liu** − *Department of Electrical Engineering and Electronics, University of Liverpool, Liverpool L69 3GJ, U.K.*

**Meiyin Liu** − *National Engineering Laboratory for VOCs Pollution Control Technology and Equipment, Guangdong Provincial Key Laboratory of Atmospheric Environment and Pollution Control, School of Environment and Energy, South China University of Technology, Guangzhou 510006, China;* orcid.org/0000-0001-7287-9710

**Longwen Chen** − *College of Light Chemical Industry and Materials Engineering, Shunde Polytechnic, Foshan 528333, China;* orcid.org/0000-0002-3404-6213

**Daiqi Ye** − *National Engineering Laboratory for VOCs Pollution Control Technology and Equipment, Guangdong Provincial Key Laboratory of Atmospheric Environment and Pollution Control, School of Environment and Energy, South China University of Technology, Guangzhou 510006, China*

Complete contact information is available at: https://pubs.acs.org/10.1021/acsenvironau.3c00008


### Author Contributions

CRediT: **Xiaomai Chen** data curation (lead), formal analysis (lead), investigation (lead), methodology (equal), visualization (lead), writing-original draft (equal), writing-review & editing (equal); **Xuefeng Shi** formal analysis (equal), investigation (equal); **Peirong Chen** formal analysis (equal), investigation (equal); **Bowen Liu** formal analysis (equal), writing-review & editing (equal); **Meiyin Liu** formal analysis (supporting), investigation (supporting); **Longwen Chen** formal analysis (supporting), investigation (supporting); **Daiqi Ye** project administration (equal), supervision (equal); **Xin Tu** conceptualization (equal), funding acquisition (equal), project administration (equal), supervision (equal), writing-review & editing; **Wei Fan** conceptualization (equal), writing-review & editing (equal); **Junliang Wu** conceptualization (lead), funding acquisition (equal), project administration (equal), supervision (equal), writing-review & editing (equal).

### Notes

The authors declare no competing financial interest.

## ACKNOWLEDGMENTS

This work was supported by the Natural Science Foundation of Guangdong Province (2020A1515010929) and the National Natural Science Foundation of China (51878292 and 51678245). X.T. gratefully acknowledges the support from the Engineering and Physical Sciences Research Council (EP/V036696).

## REFERENCES


(1) Lou, Y.; Ma, J.; Hu, W.; Dai, Q.; Wang, L.; Zhan, W.; Guo, Y.; Cao, X.-M.; Guo, Y.; Hu, P.; et al. Low-temperature methane combustion over Pd/H-ZSM-5: active Pd sites with specific electronic properties modulated by acidic sites of H-ZSM-5. *ACS Catal.* **2016**, *6*, 8127−8139.

(2) Merrin, Z.; Francisco, P. W. Unburned methane emissions from residential natural gas appliances. *Environ. Sci. Technol.* **2019**, *53*, 5473−5482.

(3) Danielis, M.; Divins, N. J.; Llorca, J.; Soler, L.; Garcia, X.; Serrano, I.; Betancourt, L. E.; Xu, W.; Rodríguez, J. A.; Senanayake, S. D.; et al. In situ investigation of the mechanochemically promoted Pd−Ce interaction under stoichiometric methane oxidation conditions. *EES Catal.* **2023**, *1*, 144−152.

(4) Schwietzke, S.; Sherwood, O. A.; Bruhwiler, L. M.; Miller, J. B.; Etiope, G.; Dlugokencky, E. J.; Michel, S. E.; Arling, V. A.; Vaughn, B. H.; White, J. W.; et al. Upward revision of global fossil fuel methane emissions based on isotope database. *Nature* **2016**, *538*, 88−91.

(5) Gatland, J. R.; Santos, I. R.; Maher, D. T.; Duncan, T.; Erler, D. V. Carbon dioxide and methane emissions from an artificially drained coastal wetland during a flood: Implications for wetland global warming potential. *J. Geophys. Res.: Biogeosci.* **2014**, *119*, 1698−1716.

(6) Gélin, P.; Primet, M. Complete oxidation of methane at low temperature over noble metal based catalysts: a review. *Appl. Catal., B* **2002**, *39*, 1−37.

(7) Yuan, X.; Meng, L.; Xu, Z.; Zheng, C.; Zhao, H. CuO quantum dots supported by $SrTiO_3$ perovskite using the flame spray pyrolysis method: enhanced activity and excellent thermal resistance for catalytic combustion of CO and $CH_4$. *Environ. Sci. Technol.* **2021**, *55*, 14080−14086.

(8) Chen, J.; Shi, W.; Zhang, X.; Arandiyan, H.; Li, D.; Li, J. Roles of $Li^+$ and $Zr^{4+}$ cations in the catalytic performances of $Co_{1-x}M_xCr_2O_4$ (M=Li, Zr; x=0−0.2) for methane combustion. *Environ. Sci. Technol.* **2011**, *45*, 8491−8497.

(9) Jiang, D.; Khivantsev, K.; Wang, Y. Low-temperature methane oxidation for efficient emission control in natural gas vehicles: Pd and beyond. *ACS Catal.* **2020**, *10*, 14304−14314.

(10) Willis, J. J.; Gallo, A.; Sokaras, D.; Aljama, H.; Nowak, S. H.; Goodman, E. D.; Wu, L.; Tassone, C. J.; Jaramillo, T. F.; Abild-Pedersen, F.; et al. Systematic structure−property relationship studies in palladium-catalyzed methane complete combustion. *ACS Catal.* **2017**, *7*, 7810−7821.

(11) Hosseiniamoli, H.; Bryant, G.; Kennedy, E. M.; Mathisen, K.; Nicholson, D.; Sankar, G.; Setiawan, A.; Stockenhuber, M. Understanding structure−function relationships in zeolite-supported Pd catalysts for oxidation of ventilation air methane. *ACS Catal.* **2018**, *8*, 5852−5863.
(12) Cargnello, M.; Jaén, J. D.; Garrido, J. C. H.; Bakhmutsky, K.; Montini, T.; Gámez, J. C.; Gorte, R.; Fornasiero, P. Exceptional activity for methane combustion over modular Pd@$CeO_2$ subunits on functionalized $Al_2O_3$. *Science* **2012**, *337*, 713−717.
(13) Wang, D.; Luo, J.; Yang, Q.; Yan, J.; Zhang, K.; Zhang, W.; Peng, Y.; Li, J.; Crittenden, J. Deactivation mechanism of multipoisons in cement furnace flue gas on selective catalytic reduction catalysts. *Environ. Sci. Technol.* **2019**, *53*, 6937−6944.
(14) Zhang, Z.; Sun, L.; Hu, X.; Zhang, Y.; Tian, H.; Yang, X. Anti-sintering Pd@silicalite-1 for methane combustion: Effects of the moisture and $SO_2$. *Appl. Surf. Sci.* **2019**, *494*, 1044−1054.
(15) Petrov, A. W.; Ferri, D.; Krumeich, F.; Nachtegaal, M.; van Bokhoven, J. A.; Krocher, O. Stable complete methane oxidation over palladium based zeolite catalysts. *Nat. Commun.* **2018**, *9*, 2545.
(16) Wang, W.; Zhou, W.; Li, W.; Xiong, X.; Wang, Y.; Cheng, K.; Kang, J.; Zhang, Q.; Wang, Y. In-situ confinement of ultrasmall palladium nanoparticles in silicalite-1 for methane combustion with excellent activity and hydrothermal stability. *Appl. Catal., B* **2020**, *276*, 119142.
(17) Petrov, A. W.; Ferri, D.; Krocher, O.; van Bokhoven, J. A. Design of stable palladium-based zeolite catalysts for complete methane oxidation by postsynthesis zeolite modification. *ACS Catal.* **2019**, *9*, 2303−2312.
(18) Losch, P.; Huang, W.; Vozniuk, O.; Goodman, E. D.; Schmidt, W.; Cargnello, M. Modular Pd/zeolite composites demonstrating the key role of support hydrophobic/hydrophilic character in methane catalytic combustion. *ACS Catal.* **2019**, *9*, 4742−4753.
(19) Li, T.; Beck, A.; Krumeich, F.; Artiglia, L.; Ghosalya, M. K.; Roger, M.; Ferri, D.; Kröcher, O.; Sushkevich, V.; Safonova, O. V.; et al. Stable Palladium Oxide Clusters Encapsulated in Silicalite-1 for Complete Methane Oxidation. *ACS Catal.* **2021**, *11*, 7371−7382.
(20) Tang, X.; Lou, Y.; Zhao, R.; Tang, B.; Guo, W.; Guo, Y.; Zhan, W.; Jia, Y.; Wang, L.; Dai, S.; et al. Confinement of subnanometric PdCo bimetallic oxide clusters in zeolites for methane complete oxidation. *Chem. Eng. J.* **2021**, *418*, 129398.
(21) Willis, J. J.; Goodman, E. D.; Wu, L.; Riscoe, A. R.; Martins, P.; Tassone, C. J.; Cargnello, M. Systematic identification of promoters for methane oxidation catalysts using size-and composition-controlled Pd-based bimetallic nanocrystals. *J. Am. Chem. Soc.* **2017**, *139*, 11989−11997.
(22) Yang, Y.; Wang, S.; Tu, X.; Hu, Z.; Zhu, Y.; Guo, H.; Li, Z.; Zhang, L.; Peng, M.; Jia, L.; et al. Atomic cerium modulated palladium nanoclusters exsolved ferrite catalysts for lean methane conversion. *Exploration* **2022**, *2*, 20220060.
(23) Yang, Y.; Zhang, L.; Guo, H.; Ding, Z.; Wang, W.; Li, J.; Zhou, L.; Tu, X.; Qiu, Y.; Chen, G.; et al. Keys Unlocking Redispersion of Reactive $PdO_x$ Nanoclusters on Ce-Functionalized Perovskite Oxides for Methane Activation. *ACS Appl. Mater. Interfaces* **2022**, *14*, 30704−30713.
(24) Shi, C.; Yang, L.; Cai, J. Cerium promoted Pd/HZSM-5 catalyst for methane combustion. *Fuel* **2007**, *86*, 106−112.
(25) Hoffmann, M.; Kreft, S.; Georgi, G.; Fulda, G.; Pohl, M.-M.; Seeburg, D.; Berger-Karin, C.; Kondratenko, E. V.; Wohlrab, S. Improved catalytic methane combustion of Pd/$CeO_2$ catalysts via porous glass integration. *Appl. Catal., B* **2015**, *179*, 313−320.
(26) Colussi, S.; Gayen, A.; Farnesi Camellone, M.; Boaro, M.; Llorca, J.; Fabris, S.; Trovarelli, A. Nanofaceted Pd-O Sites in Pd-Ce Surface Superstructures: Enhanced Activity in Catalytic Combustion of Methane. *Angew. Chem., Int. Ed.* **2009**, *48*, 8481−8484.
(27) Peng, H.; Rao, C.; Zhang, N.; Wang, X.; Liu, W.; Mao, W.; Han, L.; Zhang, P.; Dai, S. Confined ultrathin Pd-Ce nanowires with outstanding moisture and $SO_2$ tolerance in methane combustion. *Angew. Chem., Int. Ed.* **2018**, *57*, 8953−8957.
(28) Wang, N.; Sun, Q.; Bai, R.; Li, X.; Guo, G.; Yu, J. In situ confinement of ultrasmall Pd clusters within nanosized silicalite-1 zeolite for highly efficient catalysis of hydrogen generation. *J. Am. Chem. Soc.* **2016**, *138*, 7484−7487.
(29) Brun, M.; Berthet, A.; Bertolini, J. XPS, AES and Auger parameter of Pd and PdO. *J. Electron Spectrosc. Relat. Phenom.* **1999**, *104*, 55−60.
(30) Chen, S.; Li, S.; You, R.; Guo, Z.; Wang, F.; Li, G.; Yuan, W.; Zhu, B.; Gao, Y.; Zhang, Z.; et al. Elucidation of active sites for $CH_4$ catalytic oxidation over Pd/$CeO_2$ via tailoring metal−support interactions. *ACS Catal.* **2021**, *11*, 5666−5677.
(31) Monteiro, R.; Zemlyanov, D.; Storey, J.; Ribeiro, F. Turnover rate and reaction orders for the complete oxidation of methane on a palladium foil in excess dioxygen. *J. Catal.* **2001**, *199*, 291−301.
(32) Zecevic, J.; Vanbutsele, G.; de Jong, K. P.; Martens, J. A. Nanoscale intimacy in bifunctional catalysts for selective conversion of hydrocarbons. *Nature* **2015**, *528*, 245−248.
(33) Goodman, E. D.; Schwalbe, J. A.; Cargnello, M. Mechanistic understanding and the rational design of sinter-resistant heterogeneous catalysts. *ACS Catal.* **2017**, *7*, 7156−7173.
(34) Li, X.; Wang, X.; Roy, K.; van Bokhoven, J. A.; Artiglia, L. Role of water on the structure of palladium for complete oxidation of methane. *ACS Catal.* **2020**, *10*, 5783−5792.
(35) Schwartz, W. R.; Pfefferle, L. D. Combustion of Methane over Palladium-Based Catalysts: Support Interactions. *J. Phys. Chem. C* **2012**, *116*, 8571−8578.
(36) Xie, S.; Liu, Y.; Deng, J.; Zang, S.; Zhang, Z.; Arandiyan, H.; Dai, H. Efficient removal of methane over cobalt-monoxide-doped AuPd nanocatalysts. *Environ. Sci. Technol.* **2017**, *51*, 2271−2279.
(37) Duan, H.; You, R.; Xu, S.; Li, Z.; Qian, K.; Cao, T.; Huang, W.; Bao, X. Pentacoordinated $Al^{3+}$-Stabilized Active Pd Structures on $Al_2O_3$-Coated Palladium Catalysts for Methane Combustion. *Angew. Chem., Int. Ed.* **2019**, *58*, 12043−12048.
(38) Chen, J.; Zhang, G.; Wu, Y.; Hu, W.; Qu, P.; Wang, Y.; Zhong, L.; Chen, Y. Pd supported on alumina using $CePO_4$ as an additive: phosphorus-resistant catalyst for emission control in vehicles fueled by natural gas. *Ind. Eng. Chem. Res.* **2020**, *59*, 6497−6505.
(39) Zheng, Y.; Wang, L.; Zhong, F.; Cai, G.; Xiao, Y.; Jiang, L. Site-oriented design of high-performance halloysite-supported palladium catalysts for methane combustion. *Ind. Eng. Chem. Res.* **2020**, *59*, 5636−5647.
(40) Yang, S.; Maroto-Valiente, A.; Benito-Gonzalez, M.; Rodriguez-Ramos, I.; Guerrero-Ruiz, A. Methane combustion over supported palladium catalysts: I. Reactivity and active phase. *Appl. Catal., B* **2000**, *28*, 223−233.
(41) Ivanova, A.; Slavinskaya, E.; Gulyaev, R.; Zaikovskii, V.; Stonkus, O.; Danilova, I.; Plyasova, L.; Polukhina, I.; Boronin, A. Metal−support interactions in Pt/$Al_2O_3$ and Pd/$Al_2O_3$ catalysts for CO oxidation. *Appl. Catal., B* **2010**, *97*, 57−71.
(42) Tsubaki, N.; Sun, S.; Fujimoto, K. Different functions of the noble metals added to cobalt catalysts for Fischer−Tropsch synthesis. *J. Catal.* **2001**, *199*, 236−246.
(43) Ohtsuka, H.; Tabata, T. Influence of Si/Al ratio on the activity and durability of Pd-ZSM-5 catalysts for nitrogen oxide reduction by methane. *Appl. Catal., B* **2000**, *26*, 275−284.
(44) McBride, J. R.; Hass, K. C.; Weber, W. H. Resonance-Raman and lattice-dynamics studies of single-crystal PdO. *Phys. Rev. B: Condens. Matter Mater. Phys.* **1991**, *44*, 5016−5028.
(45) Su, Z.; Yang, W.; Wang, C.; Xiong, S.; Cao, X.; Peng, Y.; Si, W.; Weng, Y.; Xue, M.; Li, J. Roles of oxygen vacancies in the bulk and surface of $CeO_2$ for toluene catalytic combustion. *Environ. Sci. Technol.* **2020**, *54*, 12684−12692.
(46) Li, M.; Wang, P.; Ji, Z.; Zhou, Z.; Xia, Y.; Li, Y.; Zhan, S. Efficient photocatalytic oxygen activation by oxygen-vacancy-rich $CeO_2$-based heterojunctions: Synergistic effect of photoexcited electrons transfer and oxygen chemisorption. *Appl. Catal., B* **2021**, *289*, 120020.
(47) Hernández-Alonso, M. D.; Hungría, A. B.; Martínez-Arias, A.; Fernández-García, M.; Coronado, J. M.; Conesa, J. C.; Soria, J. EPR study of the photoassisted formation of radicals on $CeO_2$ nanoparticles


https://doi.org/10.1021/acsenvironau.3c00008
ACS Environ. Au XXXX, XXX, XXX−XXX

employed for toluene photooxidation. *Appl. Catal., B* **2004**, *50*, 167−175.
(48) Shi, X.; Chen, X.; Chen, L.; Wang, J.; Li, H.; Mao, M.; Fu, M.; Ye, D.; Jing, Z.; Wu, J. Effect of oxygen vacancy on the oxidation of toluene by ozone over Ag-Ce catalysts at low temperature. *Appl. Surf. Sci.* **2022**, *601*, 154237.
(49) Yang, J.; Hu, S.; Shi, L.; Hoang, S.; Yang, W.; Fang, Y.; Liang, Z.; Pan, C.; Zhu, Y.; Li, L.; et al. Oxygen vacancies and Lewis acid sites synergistically promoted catalytic methane combustion over perovskite oxides. *Environ. Sci. Technol.* **2021**, *55*, 9243−9254.
(50) Peng, H.; Dong, T.; Yang, S.; Chen, H.; Yang, Z.; Liu, W.; He, C.; Wu, P.; Tian, J.; Peng, Y.; et al. Intra-crystalline mesoporous zeolite encapsulation-derived thermally robust metal nanocatalyst in deep oxidation of light alkanes. *Nat. Commun.* **2022**, *13*, 295.
(51) Krcha, M. D.; Mayernick, A. D.; Janik, M. J. Periodic trends of oxygen vacancy formation and C−H bond activation over transition metal-doped $CeO_2$ (111) surfaces. *J. Catal.* **2012**, *293*, 103−115.
(52) Xiong, J.; Yang, J.; Chi, X.; Wu, K.; Song, L.; Li, T.; Zhao, Y.; Huang, H.; Chen, P.; Wu, J.; et al. Pd-Promoted $Co_2NiO_4$ with lattice Co-O-Ni and interfacial Pd-O activation for highly efficient methane oxidation. *Appl. Catal., B* **2021**, *292*, 120201.
(53) Senftle, T. P.; Van Duin, A. C.; Janik, M. J. Role of Site Stability in Methane Activation on $Pd_xCe_{1-x}O_\delta$ Surfaces. *ACS Catal.* **2015**, *5*, 6187−6199.
(54) Hornés, A.; Gamarra, D.; Munuera, G.; Fuerte, A.; Valenzuela, R.; Escudero, M.; Daza, L.; Conesa, J.; Bera, P.; Martínez-Arias, A. Structural, catalytic/redox and electrical characterization of systems combining Cu−Ni with $CeO_2$ or $Ce_{1-x}M_xO_{2-\delta}$ (M= Gd or Tb) for direct methane oxidation. *J. Power Sources* **2009**, *192*, 70−77.
(55) Carstens, J. N.; Su, S. C.; Bell, A. T. Factors affecting the catalytic activity of $Pd/ZrO_2$ for the combustion of methane. *J. Catal.* **1998**, *176*, 136−142.
(56) Gao, M.; Gong, Z.; Weng, X.; Shang, W.; Chai, Y.; Dai, W.; Wu, G.; Guan, N.; Li, L. Methane combustion over palladium catalyst within the confined space of MFI zeolite. *Chin. J. Catal.* **2021**, *42*, 1689−1699.
(57) Song, L.; Xiong, J.; Cheng, H.; Lu, J.; Liu, P.; Fu, M.; Wu, J.; Chen, L.; Huang, H.; Ye, D. In-Situ characterizations to investigate the nature of $Co^{3+}$ coordination environment to activate surface adsorbed oxygen for methane oxidation. *Appl. Surf. Sci.* **2021**, *556*, 149713.
(58) Xu, J.; Ouyang, L.; Mao, W.; Yang, X.-J.; Xu, X.-C.; Su, J.-J.; Zhuang, T.-Z.; Li, H.; Han, Y.-F. Operando and Kinetic Study of Low-Temperature, Lean-Burn Methane Combustion over a Pd/$\gamma$-Al2O3 Catalyst. *ACS Catal.* **2012**, *2*, 261−269.
(59) Chin, Y. H.; Buda, C.; Neurock, M.; Iglesia, E. Consequences of metal-oxide interconversion for C-H bond activation during $CH_4$ reactions on Pd catalysts. *J. Am. Chem. Soc.* **2013**, *135*, 15425−15442.




https://doi.org/10.1021/acsenvironau.3c00008
*ACS Environ. Au* XXXX, XXX, XXX−XXX